Nano Energy 25 (2016) 193–202

Contents lists available at ScienceDirect

Nano Energy

journal homepage: www.elsevier.com/locate/nanoen

Nitrogen-doped hierarchically porous carbon foam: A free-standing electrode and mechanical support for high-performance supercapacitors

Jizhang Chen [a], Junling Xu [a], Shuang Zhou [a], Ni Zhao [a,*], Ching-Ping Wong [a,b,**]

[a] Department of Electronic Engineering, The Chinese University of Hong Kong, New Territories, Hong Kong
[b] School of Materials Science and Engineering, Georgia Institute of Technology, Atlanta, GA 30332, United States

ARTICLE INFO

Article history:
Received 2 March 2016
Received in revised form
5 April 2016
Accepted 20 April 2016
Available online 22 April 2016

Keywords:
Hierarchically porous structure
Carbon foam
Nitrogen-doping
Nickel cobalt sulfides
Asymmetric supercapacitors

ABSTRACT

Free-standing 3D carbonaceous materials offer many advantages and therefore hold great potential for a wide range of applications. However, the synthesis of these materials often involves complicated processes that may lead to low yields and high costs. In this study, this issue is addressed through developing a facile, scalable, and cost-effective synthesis strategy. Nitrogen-doped hierarchically porous carbon foam (HP-CF) is fabricated by annealing of soft-template-casted melamine foam, and its application for supercapacitors is highlighted. The HP-CF integrates a large number of macropores and micropores, thus providing sufficient space for ion transport while offering a large amount of surface sites for energy storage, thanks to which the HP-CF exhibits a high capacitance of 238 F g^{-1} (or 11.9 F cm^{-3}). In addition, the HP-CF performs greatly when acting as the mechanical support for pseudocapacitive materials such as $NiCo_2S_4$ and Fe_2O_3, based on which an asymmetric supercapacitor (ASC, can also be described as aqueous battery) is assembled. The ASC exhibits a high energy density of 93.9 Wh kg^{-1} (or 3.55 mWh cm^{-3}) and a high power density of 21.1 kW kg^{-1} (or 799 mW cm^{-3}), among the highest reported values for ASCs.

1. Introduction

Free-standing 3-D carbon has attracted much research attention during recent years. In general, this type of materials is self-supported, mechanically flexible and compressible, electronically and thermally conductive, chemically stable, and rich in interconnected macropores. Benefiting from these advantages, 3-D carbonaceous materials have been explored for a variety of applications, such as electrochemical electrodes (*e.g.*, supercapacitors [1], batteries [2,3], fuel cells [4], and solar cells [5]), absorbers [6], and matrixes for sensors [7] and thermal energy storage [8]. Currently, the synthesis methods of free-standing 3-D carbon can be mainly classified into four categories: self-assembly of graphene oxide (GO) (*e.g.,* hydrothermal treatment [9,10], lyophilization [11,12], vacuum evaporation [13,14], and drop-casting [15]), chemical vapor deposition (CVD) [16], blowing of carbon precursors [17], and carbonization of polymer foams [18–20]. Self-assembly of GO is a widely used method; however, 3-D reduced GO (rGO) often encounters problems such as π-π restacking of rGO nanosheets and poor inter-sheet connections. Worse still, this method requires critical synthesis conditions and only produces 3-D rGO in small-scale. In order to synthesize high-quality graphene foam (GF), Cheng et al. proposed a CVD method by using Ni foams as the template [16]. This method demands careful manipulation of a complex growth process, making it difficult for commercialization. In addition, the CVD-grown graphene networks are relatively soft and can be torn easily.

To deal with the scalability problem of the previous two methods, Bando et al. synthesized 3-D strutted graphene in large quantities *via* pyrolysis of glucose assisted by a blowing agent [17]. Although 3-D carbon can be obtained, the morphology of the materials is irregular and hard to control due to the difficulty in structuring the precursor powders *via* pyrolysis. Also, the method requires a rather high processing temperature (1350 °C). Recently, it was demonstrated that 3-D carbon foams (CFs) can be fabricated by directly carbonizing commercially available polymer foams [18–20]. Despite the excellent mechanical characteristics of these CFs, their structures and properties are restricted by the raw-material –

* Corresponding author.
** Corresponding author at: Department of Electronic Engineering, The Chinese University of Hong Kong, New Territories, Hong Kong.
E-mail addresses: nzhao@ee.cuhk.edu.hk (N. Zhao), cpwong@cuhk.edu.hk (C.-P. Wong).

http://dx.doi.org/10.1016/j.nanoen.2016.04.037
2211-2855/

commercial melamine foams. An improved method to enable tuning of the material properties is highly desired.

In this study, we develop a facile, scalable, and cost-effective strategy to synthesize nitrogen-doped hierarchically porous carbon foam (designated as HP-CF) from the soft-template-casted melamine foam, and we demonstrate the application of the HP-CF in supercapacitors. Supercapacitors have been known for their excellent cycling stability and high power density, which promise diverse applications such as hybrid electric vehicles, cranes, forklifts, emergency back-up systems, *etc*. [21–24]. Since the capacitance of conventional supercapacitors, namely electric double-layer capacitors (EDLCs), depends on the surface area of the electrodes, enhancing the porosity (especially microporosity) of the electrode materials should be an effective route to enhance the supercapacitor performance. Hierarchically porous carbonaceous powders that integrate macropores and micropores have shown excellent performances for EDLCs, owing to the synergetic effect of macropores and micropores [25,26]. However, so far there have been few reports of free-standing 3D carbon materials with sufficient micropores.

Here, through templating the growth of melamine foams with structure-directing agent, we obtained HP-CF that contains not only the macropores that commonly exist in free-standing 3-D carbon materials but also a large amount of micropores. In addition, the HP-CF has a moderate density of approximately 50 mg cm^{-3}, which is 10-fold of that (approximately 5 mg cm^{-3} in average) of previously reported GFs and CFs [17,18,20,27,28]. Note that although the ultra-light-weight electrode materials can give a very high gravimetric capacitance, their volumetric capacitance is very low. For practical applications, volumetric energy density is as important if not more. Thanks to the hierarchically porous structure, the HP-CF is able to maintain a high volumetric capacitance of 11.9 F cm^{-3} while still delivering a high gravimetric capacitance of 238 F g^{-1}. In order to further improve the capacitance, we used the HP-CF as the mechanical scaffold to support the growth of pseudocapacitive materials, $NiCo_2S_4$ and graphene/porous Fe_2O_3 (denoted G-Fe_2O_3) [29], which can store and release considerably more charges than EDLC materials through redox reactions, and are used as the cathode and anode materials, respectively. The aqueous battery (called ASC in most reports) assembled from the above-mentioned electrode materials exhibits greatly improved energy and power densities, *i.e*., 93.9 wh kg^{-1}/3.55 mWh cm^{-3} at 2.25 kw kg^{-1}/84.9 mW cm^{-3}.

2. Experimental section

2.1. Synthesis of nitrogen-doped hierarchically porous carbon foam (HP-CF)

All reagents were purchased from Aldrich unless otherwise specified. Typically, 3 g paraformaldehyde, 5 g melamine and 2 g Pluronic P123 (PEG-PPG-PEG) were added to a round-bottom flask containing 10 mL 0.5 M NaOH aqueous solution, followed by stirring and refluxing at 85 °C. After 1 h reaction, the melamine resin was obtained, and was subsequently cooled down and mixed with 0.1 mL octylphenol polyoxyethylene ether (OP-10, purchased from HELM AG), 1 mL pentane and 0.3 mL formic acid under vigorous stirring. Then the as-obtained emulsion was solidified at 80 °C for 4 h to form melamine foam. The carbonization of melamine foam was carried out in a tube furnace under an Ar atmosphere. The temperature was increased at a rate of 1.5 °C min^{-1} from room temperature to 350 °C, 5 °C min^{-1} from 350 °C to 800 °C, and then held at 800 °C for 1 h. After washed in hot water and dried in an oven, the HP-CF was obtained. For comparison, a macroporous carbon foam with limited micropores was synthesized *via* a same process except for adding P123, and was denoted Ma-CF. Similarly, a microporous carbon monolith (Mi-CM) with limited macropores was synthesized by a same process except for adding OP-10 and pentane.

2.2. Synthesis of $NiCo_2S_4$ in-situ grown onto the HP-CF

The melamine resin obtained in the above section was stirred and mixed with 0.1 mL OP-10, 1 mL pentane and 0.4 mL formic acid. Then this emulsion was further mixed with 2 mL aqueous solution of 2.4 mmoL $Co(NO_3)_2$ and 1.2 mmoL $Ni(NO_3)_2$ under vigorous stirring. Subsequently, the as-obtained emulsion was solidified at 80 °C for 4 h to form a melamine foam, which was further annealed at 800 °C for 1 h under an Ar atmosphere. After that, the product was immersed into a 0.1 M Na_2S aqueous solution that was contained in a Teflon-lined stainless steel autoclave, and then the autoclave was maintained at 180 °C for 24 h. After cooling to room temperature, the product was washed with deionized water and ethanol several times, and dried at 80 °C. The final product is designated as HP-CF@$NiCo_2S_4$.

2.3. Characterization

The morphologies and elemental compositions were characterized by a field emission scanning electron microscope (FE-SEM, Quanta F400) equipped with an energy dispersive X-ray spectroscopy (EDX) detector. A FEI Tecnai F20 transmission electron microscope (TEM) equipped with an EDX detector and a HAADF detector was used to further investigate the samples and take EDX maps. Olympus BHM microscope was used to capture optical microscope images. The compression/release test was conducted by an Instron 4486 mechanical tester equipped with two flat-surface compression stages and a 100 N load cell. The X-ray diffraction (XRD) patterns were collected using a Rigaku (RU300) diffractometer with Cu Kα radiation source (λ=0.1540598 nm). Investigations of chemical compositions were performed using X-ray photoelectron spectroscopy (XPS, Physical Electronics PHI 5600). Raman spectra were recorded with a Renishaw RM-1000 Micro Raman Spectrometer. N_2 adsorption/desorption measurement was carried out by a Micromeritics ASAP 2020 instrument. The electrical conductivities were measured by sandwiching the cubic samples between two Pt foils through a two-probe method. An ICAP6300-type inductively coupled plasma (ICP) spectrometer (Thermo) was used to further analyze chemical compositions.

2.4. Electrochemical measurements

The as-synthesized HP-CF, Ma-CF, Mi-CM, and HP-CF@$NiCo_2S_4$ were used directly as electrodes. Three-electrode measurements on these materials (used as the working electrode) were performed using the Pt plate, Hg/HgO electrode, and a 3 M KOH aqueous solution as the counter electrode, reference electrode, and electrolyte, respectively. Cyclic voltammetry (CV), galvanostatic charging/discharging (GCD), and electrochemical impedance spectroscopy (EIS) tests were conducted using a VMP3 electrochemical workstation (Bio-Logic) based on the mass of the whole working electrode. Symmetric supercapacitor (SC) devices were assembled by using two HP-CFs, a 3 M KOH aqueous solution, and a filter paper as symmetric electrodes, electrolyte, and separator, respectively. For the ASC, HP-CF@$NiCo_2S_4$ and HP-CF@G-Fe_2O_3 served as the positive electrode and negative electrode, respectively. HP-CF@G-Fe_2O_3 was prepared by mixing G-Fe_2O_3 with polyvinylidene difluoride (PVDF), carbon black, and CNT at a weight ratio of 80:10:5:5 in N-methylpyrrolidone (NMP) and then coated onto a HP-CF with the equal mass, followed by vacuum

drying at 110 °C under vacuum for 12 h. Prior to the assembly of the ASC, the mass of HP-CF@$NiCo_2S_4$ and HP-CF@G-Fe_2O_3 was balanced according to: $q_+ = q_-$. Two-electrode measurements were carried out based on the total mass of the two electrodes.

3. Results and discussion

3.1. Synthesis and characterization of the HP-CF

The synthesis process of the HP-CF is summarized in Fig. 1(a). The melamine resin synthesized from melamine and paraformaldehyde was used as the carbon precursor, and its molecular formula is shown in Fig. S1. In our process, OP-10 and pentane functioned as the emulsifier and macropore-forming agent, respectively, to create macropores. P123 acted as the micropore soft template, which was consumed and introduced micropores during carbonization. Formic acid is a curing agent that facilitated the crosslinking and solidifying of melamine resin. As such, the soft-template-casted melamine foam was produced and subsequently carbonized to form the HP-CF (see photographs in Fig. S2). Unlike other hierarchically porous carbon obtained from pyrolyzing the biomass, polymers, and C-rich salts [25,26,30], the HP-CF preserves its integrity after pyrolysis, *i.e.*, being self-supported. The SEM images of the HP-CF with different magnifications are shown in Fig. 1b to d. Fig. 1b and c reveal that the HP-CF has a foam-like structure, in which abundant macropores are connected with each other. Fig. 1(d) magnifies the framed area in Fig. 1(c) and shows that the walls of the HP-CF also possess an interconnected macroporous network. The optical microscope image of the HP-CF is shown in Fig. 1(e), further confirming its foam-like structure. In addition to these macropores, the HP-CF is rich in mircopores, as shown from the TEM image in Fig. 1(f). In particular, these micropores can considerably enhance the EDLC performance [25,26,31]. The density of the HP-CF was measured to be ~50 mg cm^{-3}, which corresponds to a porosity of 97.2% taking the bulk density of carbon as 1.8 g cm^{-3}. Thanks to such a high porosity, the HP-CF is flexible and compressible, as illustrated by the photographs in Fig. 1(g) and (h). The compression/release test result is shown in Fig. S3. The HP-CF can bear a large compression ratio to 50% and almost recover to its original shape with a plastic deformation of less than 5%. Besides, the HP-CF can accommodate a remarkable compressive stress of 0.163 MPa without collapse. In addition to the HP-CF, we have also synthesized (1) macroporous carbon foam (Ma-CF) with limited micropores and (2) microporous carbon monolith (Mi-CM) with limited macropores, for comparison with HP-CF. The photographs, SEM images, and optical micrographs of Ma-CF and Mi-CM are shown in Fig. S2.

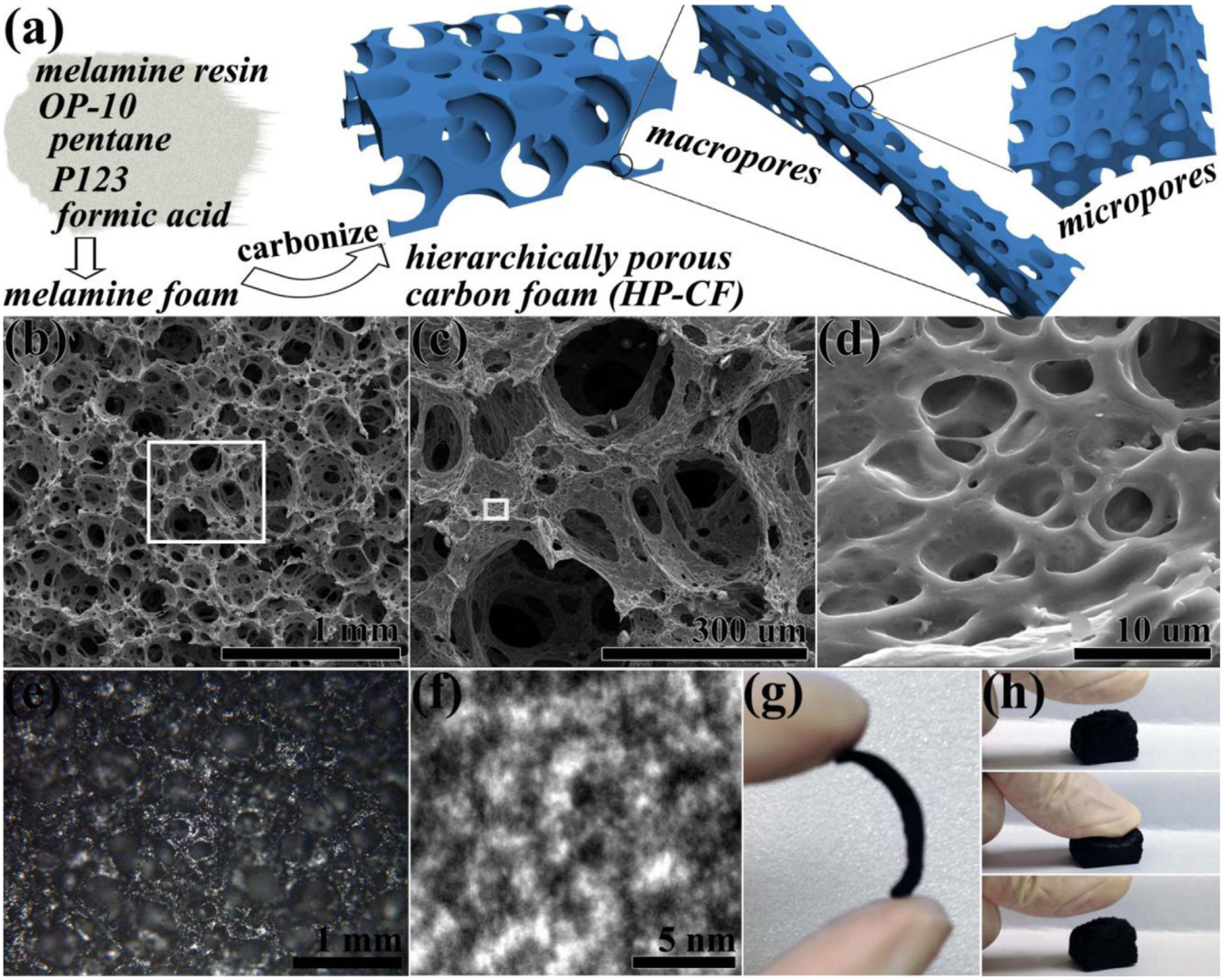

Fig. 1. (a) Illustration of the fabrication process, (b–d) SEM images with different magnifications, (e) optical microscope image, (f) TEM image, and (g, h) photographs of the HP-CF.

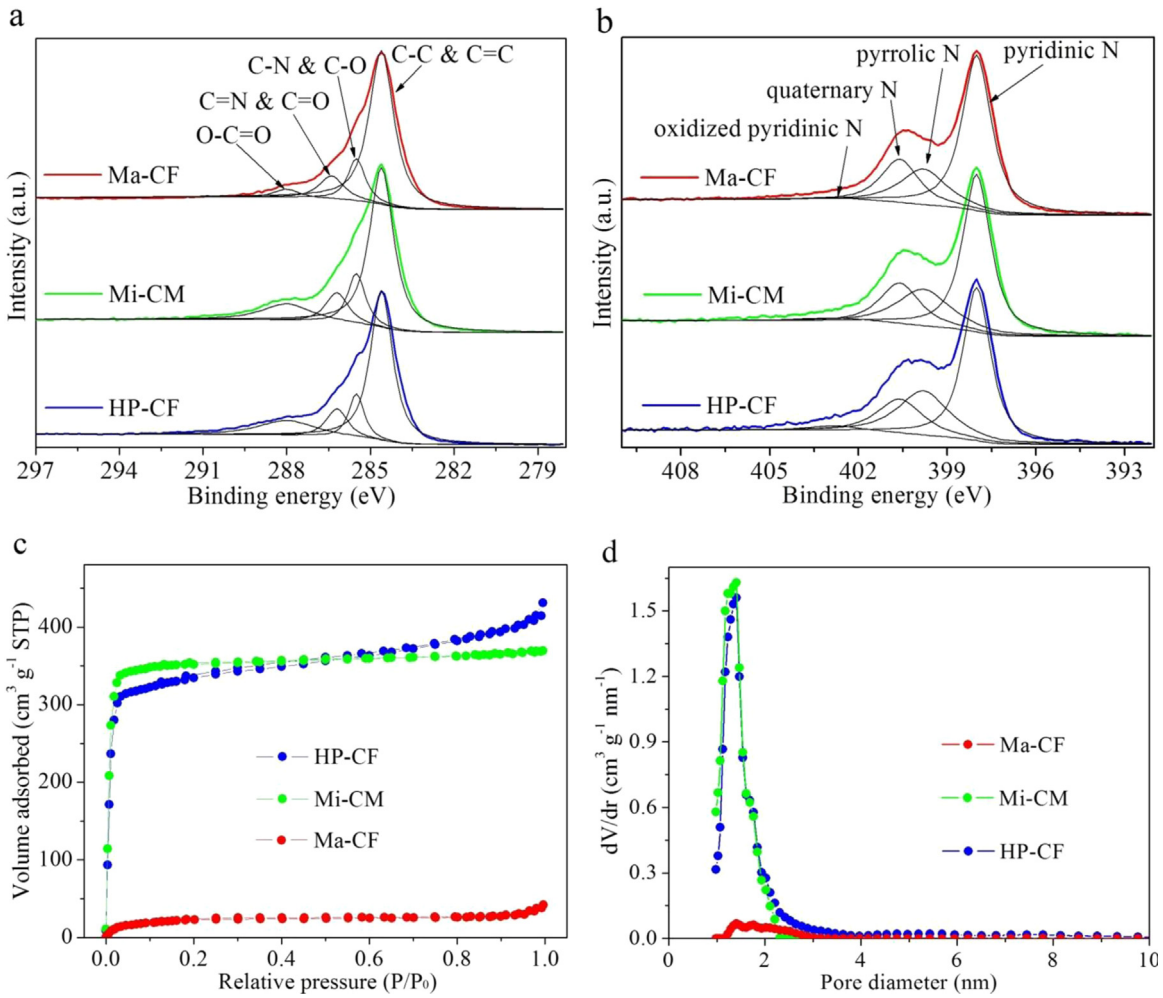

Fig. 2. (a) C 1s and (b) N 1s high-resolution XPS spectra, (c) nitrogen adsorption/desorption isotherms, and (d) DFT pore-size distributions of the Ma-CF, Mi-CM, and HP-CF.

The crystal structures of the three carbonaceous materials were measured by wide-angle XRD, as shown in Fig. S4. Two broad peaks at around 26° and 43° are observed for all the materials, which can be readily indexed as the typical (002) and (101) planes of graphitic materials. These broad peaks imply the Ma-CF, Mi-CM, and HP-CF have only a short-range order. To determine the chemical contents and valence states in these carbonaceous materials, we carried out the XPS measurements. The survey XPS spectra in Fig. S5a clearly demonstrate the presences of C, N, and O elements. The deconvolutions of the C1s spectra are exhibited in Fig. 2(a). The most pronounced peak located at 284.6 eV is characteristic of the sp^2 graphitic lattice, and the other peaks at 285.5, 286.2, and 288 eV are associated with C–N (& C–O), C=N (& C=O), and O-C=O functional groups, respectively [19]. In Fig. 2(b), the N1s spectra can be deconvoluted into four individual peaks that are assigned to pyridinic N (398.0 eV), pyrrolic N (399.8 eV), quaternary N (400.6 eV), and oxidized pyridinic N (402.8 eV), respectively [31,32]. In addition, the O1s spectra (Fig. S5b) reveal the existences of C=O quinone groups (530.6 eV), C–OH phenol groups & C–O–C ether groups (531.6 eV), and absorbed water (534.0 eV) [19]. The atomic ratios according to the XPS measurements are summarized in Table S1, revealing that the nitrogen contents in the Ma-CF, Mi-CM, and HP-CF are 20.9, 19.4, and 18.7 wt%, respectively. Besides, the characteristics of high nitrogen doping are corroborated by the EDX spectra in Fig. S6. The high nitrogen content is inherited from the ~39 wt% nitrogen in the precursor melamine resin (Fig. S1). Previous studies suggest that N-doping can enhance the capacitance of carbonaceous materials through the following mechanisms: (1) N can donate extra electrons that increase the electronic conductivity; (2) N-functionalities can undergo redox reactions, thus providing extra pseudocapacitances; and (3) N-functionalities can improve the surface wettability and therefore improve the electrode/electrolyte interface [18,27,33]. We further characterized the Ma-CF, Mi-CM, and HP-CF by Raman analysis (Fig. S7) and found all the materials exhibit a broad disorder-induced D band at ~1350 cm^{-1} and a broad in-plane vibrational G band at ~1560 cm^{-1} [25,26,34]. The I_D/I_G ratios of Ma-CF, Mi-CM, and HP-CF are 1.07, 1.21 and 1.15, respectively. Such high values imply a high degree of disorder, due likely to the high degree of N-doping and low carbonization temperature (800 °C).

To characterize the porous structures, N_2 adsorption/desorption measurements were conducted and the obtained isotherms are shown in Fig. 2(c). The Ma-CF exhibits a type II (IUPAC classification) isotherm, while the Mi-CM and HP-CF present type I isotherms. Note that the type I and II isotherms are indicative of microporous and macroporous structures, respectively. Based on the $P_0 < 0.3$ range of the isotherms, the Brunauer–Emmett–Teller (BET) surface area of the HP-CF is estimated to be 1175 $m^2 g^{-1}$, comparable to 1231 $m^2 g^{-1}$ of the Mi-CM and much higher than 83 $m^2 g^{-1}$ of the Ma-CF. Moreover, the surface area of the HP-CF is much higher than those of previously reported CFs, *e.g.*, 268 $m^2 g^{-1}$ of elastic CF [18], 299.4 $m^2 g^{-1}$ of CF/N-doped CNT [28], and 345 $m^2 g^{-1}$ of CO_2-activated CF [20]. The corresponding pore-size distribution is estimated from the adsorption branches of the isotherms based on a density functional theory (DFT) model and

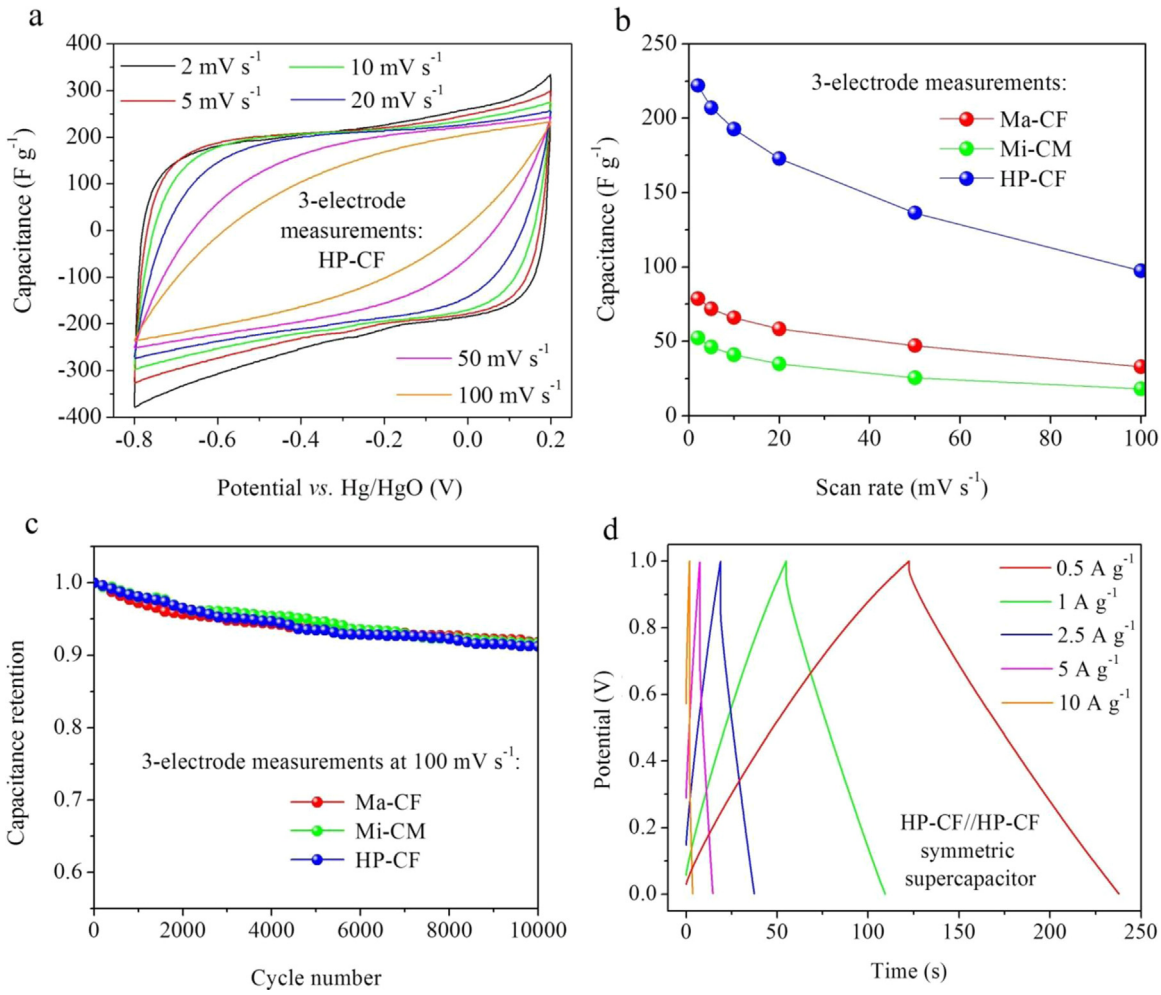

Fig. 3. (a) CV curves of the HP-CF. (b) Rate capabilities and (c) cycling performance of the HP-CF in comparison with the Ma-CF and Mi-CM. (d) GCD curves of the HP-CF//HP-CF SC.

shown in Fig. 2(d). The HP-CF and Mi-CM have a similarly high micro-porosity, much higher than that of the Ma-CF. The micropores in the HP-CF and Mi-CM are created by the soft template P123, while the micropores in the Ma-CF are produced through gas (*e.g.*, CO, N_2, and NH_3) release during carbonization. The high pore volume of 0.571 $cm^3\ g^{-1}$ of the HP-CF is favorable for charge storage.

3.2. Electrochemical measurements of the HP-CF

In addition to the superior morphological and structural characteristics, the HP-CF possesses a high electrical conductivity of 6.58 S m^{-1} (Fig. S8). These properties together make HP-CF a promising candidate as a self-supported and binder-free electrode for supercapacitors. We therefore characterized the rate-dependent CV curves of the HP-CF, Ma-CF, and Mi-CM in a KOH aqueous electrolyte with the scan rate ranging from 2 to 100 mV s^{-1}. As shown in Figs. 3(a) and S9, the CV curves at the low scan rates are similar to the rectangular CV characteristics of typical EDCL materials. (The small deviation from the rectangular shape arises from the pseudocapacitive capacitance introduced by the N-and O-functional groups.) When the scan rate is progressively increased, larger deviation from the rectangular shape is observed in the CV curves, due to stronger electrochemical polarizations at higher scan rates.

The rate capability of the three materials is summarized in Fig. 3(b) (see calculation details in Supporting Information). The capacitances of the HP-CF at 2, 10, and 50 mV s^{-1} are 222.0, 192.7, and 136.3 F g^{-1}, respectively, much higher than those of the Ma-CF and Mi-CM. These values are also higher than recently reported self-supported and binder-free CF-based EDLC materials, such as CF/N-doped CNT (133 F g^{-1}) [28], N-doped CF/OMC (203 F g^{-1}) [27], and CO_2-activated CF (40 F g^{-1}) [20]. Moreover, benefiting from its moderate density, the HP-CF exhibits a high volumetric capacitance of 11.1 F cm^{-3}, approximately 9-fold higher than those of the CF/N-doped CNT [28], N-doped CF/OMC [27], and elastic CF [18], 13-fold higher than that of the strutted graphene [17], and 33-fold higher than that of the CO_2-activated CF [20]. Note that these volumetric capacitances are based on the bulk density, not the particle density used in many other reports [33], as the former is more relevant to practical applications. Cycling stability is another important parameter. Fig. 3(c) shows the capacitance retention as a function of the cycle number, demonstrating that the HP-CF can maintain 91.2% of its initial capacitance even after 10,000 cycles. The electrochemical behaviors were further investigated by EIS measurements, and the recorded Nyquist plots are shown in Fig. S10. We found that the HP-CF shows significantly lower impedances compared with other EDLC electrodes [13,14,35,36].

By sandwiching two HP-CF electrodes in a KOH aqueous electrolyte, a symmetric supercapacitor (SC) is assembled. In Fig. 3(d), the GCD curves show typical EDLC triangle shapes and low resistance-related voltage drops. The capacitance of the SC device is 59.4 F g^{-1} (corresponding to 237.6 F g^{-1} for a single HP-CF) at 0.5 A g^{-1}, and maintains at 70.3% of this value when the current

density is increased to 20-fold. The CV curves and cycling performance of the SC device are shown in Fig. S11 and S12, revealing a high capacitance of 58.2 F g^{-1} at 2 mV s^{-1} and an excellent capacitance retention of 91.5% after 10,000 cycles, respectively. Herein, it is seen that the capacitance of the HP-CF at 2 mV s^{-1} tested in a SC configuration is slightly higher than that tested in a three-electrode configuration. This phenomenon can be due to several reasons: (1) the ionic resistance of the electrolyte is much lower in the SC configuration, owing to much lower distance (1–2 μm) between two HP-CFs as compared to that (1–2 cm) between the HP-CF and reference electrode in the three-electrode configuration; (2) the scan rate of 2 mV s^{-1} under SC configuration should actually be equivalent to the 1 mV s^{-1} scan rate under three-electrode configuration. Impressively, although not containing extra mechanical support or conductive agent, the HP-CF outperforms most of newly reported EDLC materials, such as N-doped graphene (210 F g^{-1}) [37], hollow carbon nanospheres (201 F g^{-1}) [38], porous interconnected carbon nanosheets (150 F g^{-1}) [25], graphene sponge (57 F g^{-1}) [39], as summarized in Table S2. The excellent electrochemical performances of the HP-CF are mainly attributed to its free-standing hierarchically porous structure and chemical composition. Firstly, the densely distributed and interconnected macropores facilitate ion diffusion in the electrolyte throughout the HP-CF. Secondly, the presence of abundant micropores largely increases the active area for charge storage. Thirdly, nitrogen-doping improves the electronic conductivity, enhances the surface wettability, and provides an extra pseudocapacitance. Lastly, the elimination of binders reduces the interface resistance.

3.3. HP-CF@$NiCo_2S_4$

Thanks to its unique morphology and structure, the HP-CF not only performs greatly as an electrode, but can also serve as a mechanical scaffold to support the growth of pseudocapacitive materials on the foam, so that its capacitance can be dramatically improved. Moreover, pseudocapacitive materials can be used to construct aqueous ASCs that increase the operating potential of aqueous EDLCs from approximately 1.0 V to 1.7 V, thanks to which the corresponding energy and power densities can be significantly enhanced [40–54]. In this study, we have *in-situ* grown $NiCo_2S_4$ on the HP-CF, as schematically illustrated in Fig. 4(a). $NiCo_2S_4$ is chosen since it has high electronic conductivity and rich redox couples, and is a great cathode material for ASC devices [55–60]. To fabricate the HP-CF@$NiCo_2S_4$ hybrid structure, we added Co^{2+} and Ni^{2+} nitrates to the melamine resin, while keeping other experimental conditions nearly identical to those used for synthesizing the HP-CF. During carbonization, Co^{2+} and Ni^{2+} were reduced by carbon to the metallic Co and Ni. After that, Co and Ni were *in-situ* converted to $NiCo_2S_4$ through a hydrothermal reaction with S^{2-}.

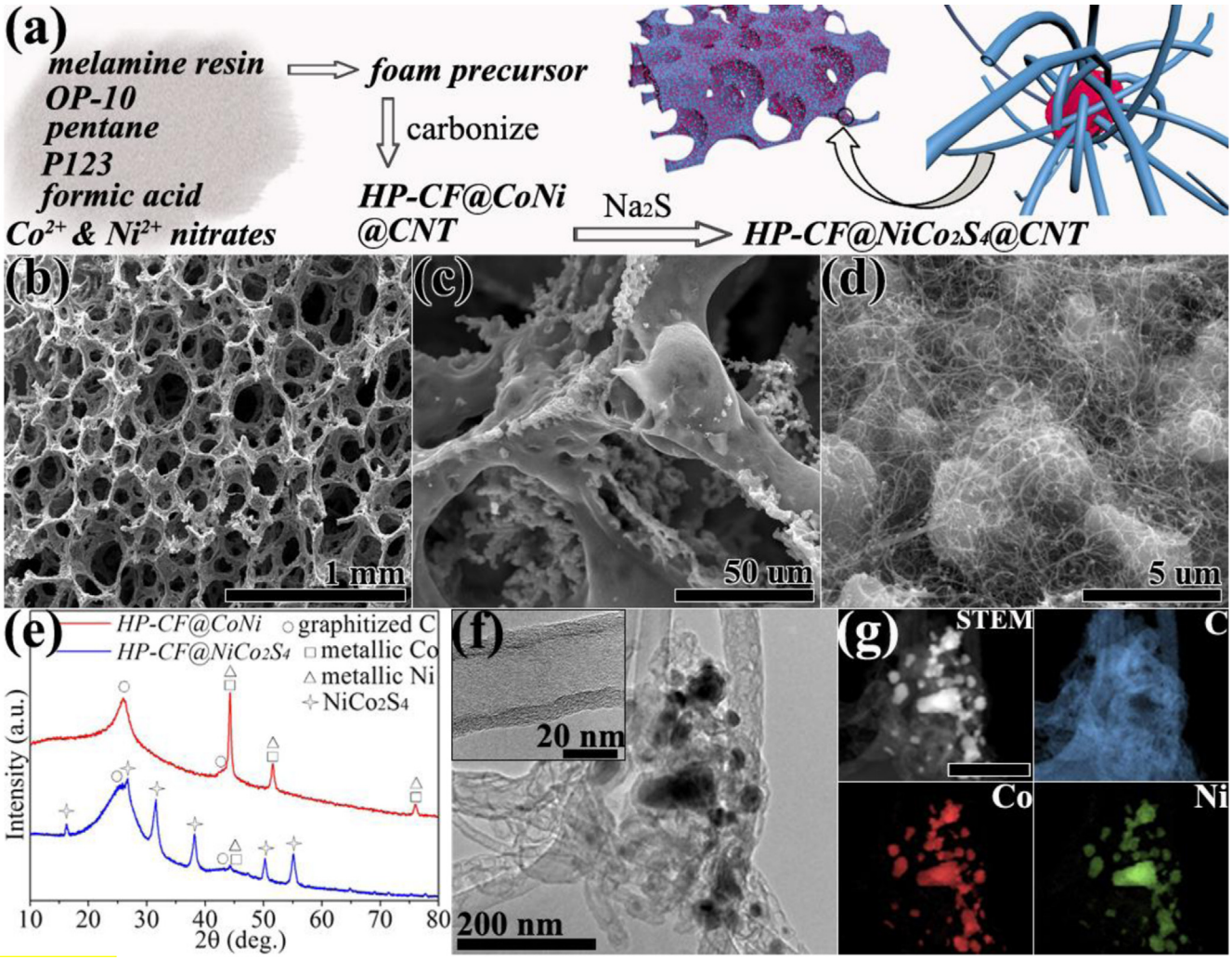

Fig. 4. (a) Illustration of the fabrication process and (b–d) SEM images with different magnifications of the HP-CF@$NiCo_2S_4$. (e) XRD patterns of the HP-CF@CoNi obtained after carbonization and the final product HP-CF@$NiCo_2S_4$. (f) TEM images, (g) STEM image and EDX elemental maps (scale bar: 200 nm) of the HP-CF@$NiCo_2S_4$.

The HP-CF@$NiCo_2S_4$ fabricated through the above routine retains the original foam-like morphology of the HP-CF (Fig. 4b and S13), with $NiCo_2S_4$ particles anchored on the surface of the HP-CF (Fig. 4 (c)). Interestingly, the magnified SEM image in Fig. 4(d) shows that the $NiCo_2S_4$ particles are wrapped by carbon nanotubes (CNTs), owing to the catalytic effects of Co and Ni. The photographs in Fig. S14 display a self-supporting characteristic. In Fig. 4(e), the conversion from metallic Co (JCPDS 15–0806) and Ni (JCPDS 70–1849) to cubic phase $NiCo_2S_4$ (JCPDS 43–1477) is evidenced by the XRD patterns, in which although some minor peaks belonging to Co and Ni exist in the final product, their intensities are extremely low compared to that of $NiCo_2S_4$. The formation of $NiCo_2S_4$ was further suggested by the XPS spectra in Fig. S15. The TEM images in Fig. 4(f) suggest that $NiCo_2S_4$ is wrapped by CNTs that have a multiwall morphology. We further employed scanning transmission electron microscopy (STEM) and EDX mapping to study the elemental distribution in the HP-CF@$NiCo_2S_4$ (Fig. 4g). From the STEM image, $NiCo_2S_4$ particles are observed to be encapsulated into the carbon matrix, which can be further verified by the EDX maps of Co, Ni, and C elements. Weight ratio of $NiCo_2S_4$ in the HP-CF@$NiCo_2S_4$ structure is estimated to be 61.08 wt% based on the XPS result, while the value becomes 47.02 wt% according to the EDX measurement (Fig. S16). Given that both characterization techniques are surface sensitive (especially for XPS), we further used ICP analysis to determine the weight percentage of the $NiCo_2S_4$ in the HP-CF@$NiCo_2S_4$, and the result suggest a weight ratio of 42.94 wt%.

In Fig. 5(a), CV curves of the HP-CF@$NiCo_2S_4$ in a KOH aqueous electrolyte show typical redox peaks that are distinct from the original curves of pure HP-CF, suggesting that the electrochemical behavior of HP-CF@$NiCo_2S_4$ is dominated by the $NiCo_2S_4$. The pseudocapacitance of $NiCo_2S_4$ mainly originates from Co^{2+}/Co^{3+} and Ni^{2+}/Ni^{3+} redox couples, and the corresponding reactions are generally proposed as: [55]

$$NiCo_2S_4 + 2OH^- \leftrightarrow NiS_{2x}OH + Co_2S_{4-2x}OH + 2e^- \quad (1)$$

Since the conversions of Co^{2+}/Co^{3+} and Ni^{2+}/Ni^{3+} occur at a similar potential, only one pair of redox peaks are distinct in the CV curves. In order to make a comparison with other reports, here we use $F\,g^{-1}$ (capacitance) rather than $mAh\,g^{-1}$ (capacity) to evaluate the electrochemical performance. The capacitances of the HP-CF@$NiCo_2S_4$ are calculated to be 599.2 and 427.0 $F\,g^{-1}$ at 2 and 20 $mV\,s^{-1}$, respectively, manifesting high capacitances and great rate capabilities. It is worth noting that these capacitances are based on the total mass of the HP-CF and $NiCo_2S_4$ and are markedly superior as compared to those of the recently reported free-standing 3-D carbon-supported pseudocapacitive materials such as GF/CNT/MnO_2 (250 $F\,g^{-1}$ at 10 $mV\,s^{-1}$) [53], CF/$NiCo_2S_4$ nanosheets (382 $F\,g^{-1}$ at 2 $A\,g^{-1}$) [47], 3D macroporous graphene/MnO_2 (389 $F\,g^{-1}$ at 1 $A\,g^{-1}$) [14], and CF/MnO_2 (43.2 $F\,g^{-1}$ at 0.5 $A\,g^{-1}$) [61]. Note that the above-mentioned capacitance values are based on the total mass of carbon and pseudocapacitive materials. The contributions of the HP-CF to the total capacitances (C_{total}) at different scan rates are estimated by

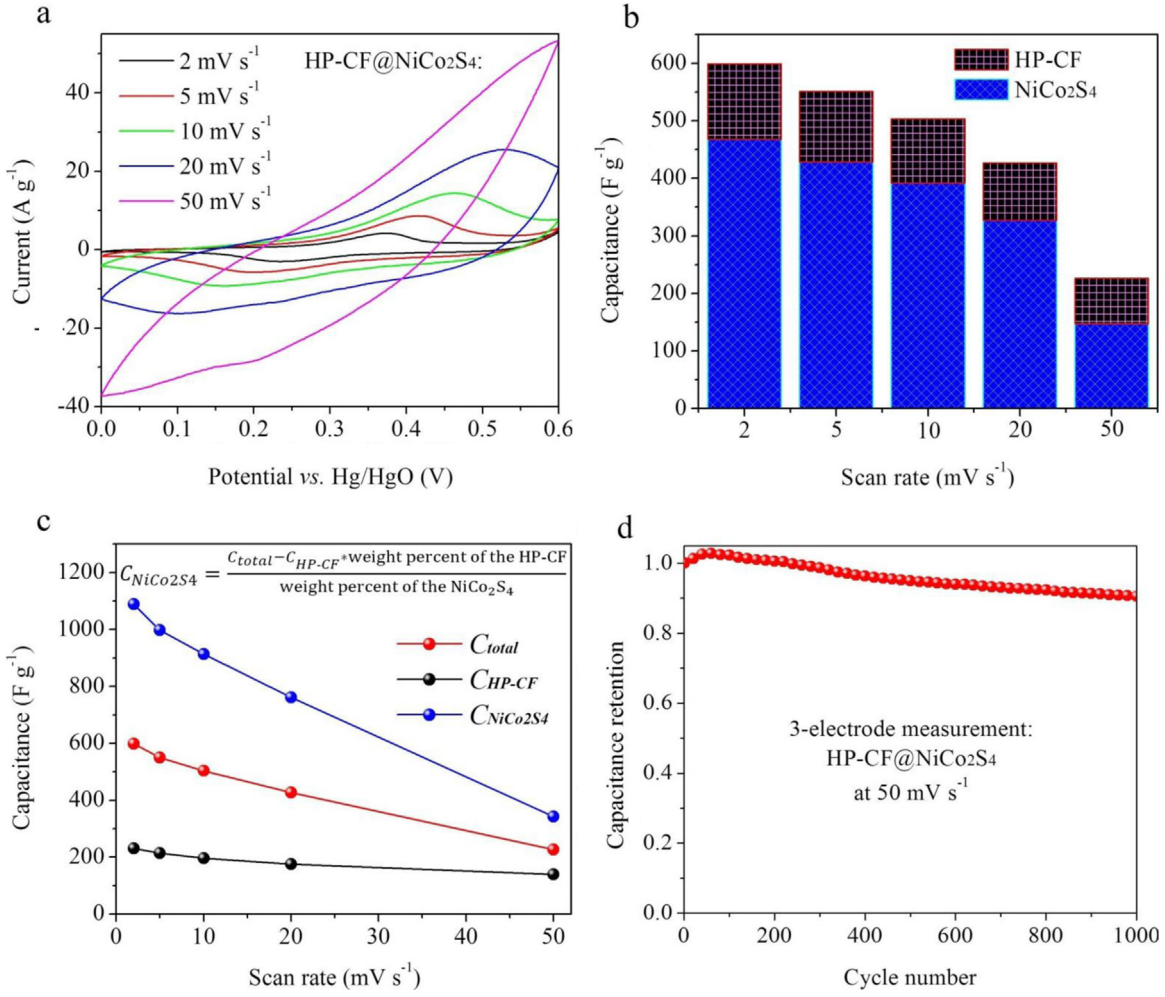

Fig. 5. (a) CV curves of the HP-CF@$NiCo_2S_4$ at various scan rates. (b) Capacitance contributions of the HP-CF and $NiCo_2S_4$ at different scan rates. (c) Evolutions of the C_{total}, $C_{HP\text{-}CF}$, and $C_{NiCo2S4}$ as a function of the scan rate. (d) Cycling performance of the HP-CF@$NiCo_2S_4$ at 50 $mV\,s^{-1}$.

multiplying $C_{HP\text{-}CF}$ and the weight percent of the HP-CF in HP-CF@$NiCo_2S_4$, where $C_{HP\text{-}CF}$ represents the capacitance of a neat HP-CF under the same potential window (Fig. S17a). Accordingly, the contributions of the $NiCo_2S_4$ can be estimated by deducting that of the HP-CF from the C_{total}. In Fig. 5(b) and S17b to S17f, it can be observed that the HP-CF contributes to higher ratios when the scan rate is increased, which is a comprehensible phenomenon as pure-surface EDLC behaviors are much more kinetically favored than diffusion-related pseudocapacitive ones. Herein, the capacitance ratio of the $NiCo_2S_4$ only drops from 0.780 to 0.649 as the scan rate goes up from 2 to 50 mV s^{-1}, implying a great rate performance, which can also by confirmed by Fig. S18 using a classic power-law equation [62–64]. Notably, the highest capacitance of the $NiCo_2S_4$ ($C_{NiCo2S4}$) is estimated to be 1088.7 F g^{-1} at 5 mV s^{-1} (Fig. 5c), superior to other electrodes based on the same material system, *e.g.*, $NiCo_2S_4$ hollow prisms (895.2 F g^{-1}) [65], tube-like $NiCo_2S_4$ (1048 F g^{-1}) [57], $NiCo_2S_4$ hollow hexagonal nanoplates (437 F g^{-1}) [60], and $NiCo_2S_4$ nanotube arrays (738 F g^{-1}) [66]. The cycling performance of the HP-CF@$NiCo_2S_4$ is depicted in Fig. 5(d). A high capacitance retention of 90.5% is obtained after 1 000 cycles, indicating a great cycling stability. It is also observed that the capacitance of HP-CF@$NiCo_2S_4$ rises first and then falls. The capacitance rise is owing to the "activation" of $NiCo_2S_4$, *i.e.*, parts of the $NiCo_2S_4$ were initially inactive but then started to contribute to the electrochemical process after a few cycles. SEM images of the HP-CF and HP-CF@$NiCo_2S_4$ after cycles (Fig. S19) show little morphological changes as compared to those before cycles, indicating high structural stability of these two products and strong adhesion of $NiCo_2S_4$ to the HP-CF.

The superior performance of the HP-CF@$NiCo_2S_4$ can be ascribed to the following three factors. Firstly, $NiCo_2S_4$ is *in-situ* grown on the HP-CF with a strong adhesion, eliminating the usage of binders and improving electron conduction between HP-CF to $NiCo_2S_4$. Secondly, the hierarchically porous structure of the HP-CF provides a hierarchical network for effective transport of electrolyte ions to the redox sites of $NiCo_2S_4$. Thirdly, the CNT wrapping further facilitates electron transport and buffers volumetric changes during repeated cycles.

3.4. HP-CF@$NiCo_2S_4$//HP-CF@G-Fe_2O_3 ASC

To further evaluate the HP-CF@$NiCo_2S_4$, we have fabricated ASC devices using HP-CF@$NiCo_2S_4$ and HP-CF@G-Fe_2O_3 as the cathode and anode, respectively. The HP-CF@G-Fe_2O_3 is prepared by pasting G-Fe_2O_3 onto a HP-CF and its SEM and CV curves are shown in Fig. S20. Because the potential windows of G-Fe_2O_3 and $NiCo_2S_4$ are compatible, the ASC can deliver a high open-circuit voltage of 1.7 V, as shown in Fig. 6(a) and S21. These CV curves reveal typical redox profiles and a relatively high capacitance retention of 50.2% when the scan rate is increased from 5 to 50 mV s^{-1}. When cycled at 50 mV s^{-1}, our ASC can maintain 81.1% of its initial capacitance after 1 000 cycles (Fig. S22). Fig. 6(b) shows GCD curves of our ASC at various current densities. These curves are nonlinearly correlated with the potential, indicating pseudocapacitive behaviors. As

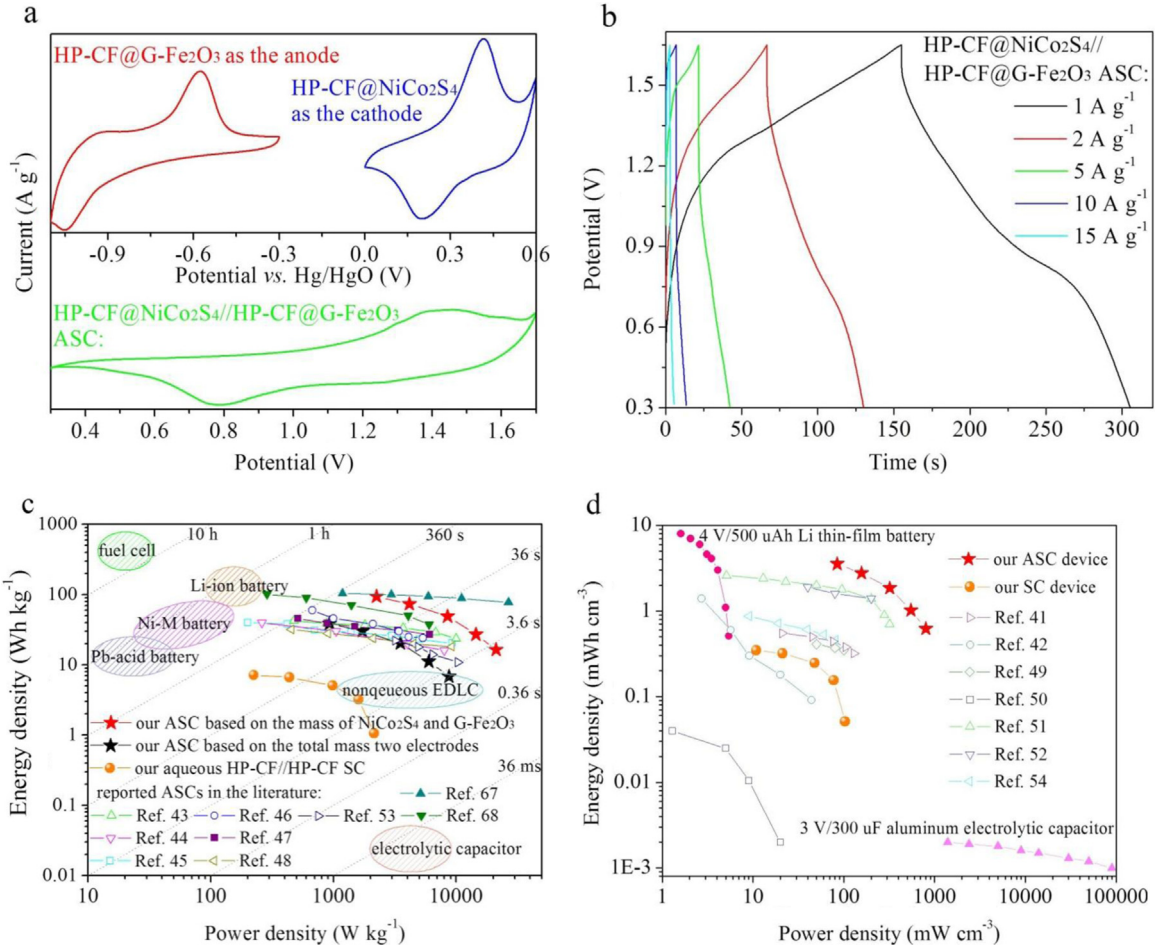

Fig. 6. (a) CV curves of the anode HP-CF@G-Fe_2O_3, cathode HP-CF@$NiCo_2S_4$, and the HP-CF@$NiCo_2S_4$//HP-CF@G-Fe_2O_3 ASC at 5 mV s^{-1}. (b) GCD profiles of the ASC at different current densities. (c) Gravimetric Ragone plots of energy density *vs.* average power density for our devices in comparison with other state-of-art ASCs. Note that all the data from other reports are based on the mass of active materials without considering the mass of mechanical supports, *e.g.*, Ni foams. (d) Volumetric Ragone plots of our devices in comparison with other reports. Note that the volumes of two HP-CFs and a separator were considered when calculating the total volume of our devices.

the current density increases from 1, 5, to 15 A g^{-1}, the specific capacitance of the ASC decreases from 118.2, 102.3, to 57.9 F g^{-1}, respectively, exhibiting superior rate capability. The ASC also manifests a low charge transfer impedance of 16.1 Ω (Fig. S23) and slow self-discharge behavior (Fig. S24).

Given that energy density and power density are two crucial factors for practical applications, we provide both gravimetric and volumetric Ragone plots of the ASC and HP-CF//HP-CF SC in Fig. 6 (c) and (d), where the performance of the devices are compared with those of the recently reported ASCs. To be consistent with other literature, we first compare the performance excluding the mass of the mechanical support. The highest gravimetric energy density of our ASC is 93.9 Wh kg^{-1} at 2 246 W kg^{-1}, while the highest power density is 21,127 W kg^{-1} at 16.4 Wh kg^{-1}, among the best ASCs ever reported [67,68], and surpassing most of the ASCs based on metal oxides, sulfides, and hydroxides [43–48,53], as listed in Fig. 6(c). It should be noted that heavy Ni foams were used as the mechanical support in most of ASCs, making the actual energy and power densities (calculated based on the total mass of the active material and mechanical support) of the devices much lower than those reported values (calculated based on only the mass of the active material). The mechanical support HP-CF used in the present study is much lighter than conventional Ni foams; and it also contributes a high EDLC. Therefore, even including the mass of the two HP-CFs in the total mass of the ACS, we can still extract a high energy density of 38.8 Wh kg^{-1} and power density of 8 737 W kg^{-1}, comparable to those reported values excluding the mass of the mechanical support of ASCs. Moreover, the ASC delivers a high volumetric energy density of 3.55 mWh cm^{-3} and power density of 799 mW cm^{-3} (Fig. 6d), much higher than those of previously reported ASCs [41,42,49–52,54]. Fig. 6(c) and (d) also indicate that the energy and power densities of HP-CF//HP-CF SCs can be significantly enhanced through decorating HP-CFs with $NiCo_2S_4$ and G-Fe_2O_3 and thus constructing ASCs. Three ASCs connected in series can be used to power 20 blue LEDs, as demonstrated in the supplementary video.

Supplementary material related to this article can be found online at http://dx.doi.org/10.1016/j.nanoen.2016.04.037.

4. Conclusion

In summary, we have developed a facile, scalable, and cost-effective synthesis strategy to fabricate free-standing nitrogen-doped carbon foam and demonstrated its application in realizing binder-free supercapacitors. Through templating the growth of melamine foam with a structure-directing agent, we obtained the HP-CF that contains not only the macropores that commonly exist in free-standing 3-D carbon materials but also a large amount of micropores. Such hierarchically porous structure facilitates charge transport while offering a large amount of surface sites for energy storage. Consequently, the HP-CF exhibits high capacitance. In addition, the HP-CF performs greatly when acting as the mechanical support for pseudocapacitive materials such as $NiCo_2S_4$ and Fe_2O_3. In particular, the CNT-wrapped *in-situ* grown $NiCo_2S_4$ exhibits a high capacitance of 1089 F g^{-1}, as well as great rate capability and superior long-term cyclability. The aqueous ASC assembled from the HP-CF@$NiCo_2S_4$ cathode and HP-CF@G-Fe_2O_3 anode exhibits very high gravimetric and volumetric energy/power densities as compared to the reported state-of-the-art ASCs. The synthetic method demonstrated in this work can be extended to other material systems, which may not only improve the performance of energy storage devices, but also enable new device applications.

Acknowledgements

This work was supported by Research Grants Council of Hong Kong (General Research Fund, No. 417012, RGC-NSFC, No. N_CUHK450/13, and TRS, No. T23–407/13 – N).

Appendix A. Supporting information

Supplementary data associated with this article can be found in the online version at http://dx.doi.org/10.1016/j.nanoen.2016.04.037.

References

[1] X. Cao, Z. Yin, H. Zhang, Energy Environ. Sci. 7 (2014) 1850–1865.
[2] V. Chabot, D. Higgins, A. Yu, X. Xiao, Z. Chen, J. Zhang, Energy Environ. Sci. 7 (2014) 1564–1596.
[3] M.C. Lin, M. Gong, B. Lu, Y. Wu, D.Y. Wang, M. Guan, M. Angell, C. Chen, J. Yang, B.J. Hwang, H. Dai, Nature 520 (2015) 325–328.
[4] Z.S. Wu, S. Yang, Y. Sun, K. Parvez, X. Feng, K. Mullen, J. Am. Chem. Soc. 134 (2012) 9082–9085.
[5] Y. Xue, J. Liu, H. Chen, R. Wang, D. Li, J. Qu, L. Dai, Angew. Chem., Int. Ed. 51 (2012) 12124–12127.
[6] Y. Shen, Q. Fang, B. Chen, Environ. Sci. Technol. 49 (2015) 67–84.
[7] H.B. Yao, J. Ge, C.F. Wang, X. Wang, W. Hu, Z.J. Zheng, Y. Ni, S.H. Yu, Adv. Mater. 25 (2013) 6692–6698.
[8] K. Lafdi, O. Mesalhy, A. Elgafy, Carbon 46 (2008) 159–168.
[9] Y.X. Xu, K.X. Sheng, C. Li, G.Q. Shi, ACS Nano 4 (2010) 4324–4330.
[10] Y. Zhao, J. Liu, Y. Hu, H. Cheng, C. Hu, C. Jiang, L. Jiang, A. Cao, L. Qu, Adv. Mater. 25 (2013) 591–595.
[11] L. Qiu, J.Z. Liu, S.L. Chang, Y. Wu, D. Li, Nat. Commun. 3 (2012) 1241–1247.
[12] H. Sun, Z. Xu, C. Gao, Adv. Mater. 25 (2013) 2554–2560.
[13] Z. Niu, J. Chen, H.H. Hng, J. Ma, X. Chen, Adv. Mater. 24 (2012) 4144–4150.
[14] B.G. Choi, M. Yang, W.H. Hong, J.W. Choi, Y.S. Huh, ACS Nano 6 (2012) 4020–4028.
[15] S.H. Lee, H.W. Kim, J.O. Hwang, W.J. Lee, J. Kwon, C.W. Bielawski, R.S. Ruoff, S. O. Kim, Angew. Chem., Int. Ed. 49 (2010) 10084–10088.
[16] Z. Chen, W. Ren, L. Gao, B. Liu, S. Pei, H.M. Cheng, Nat. Mater. 10 (2011) 424–428.
[17] X. Wang, Y. Zhang, C. Zhi, X. Wang, D. Tang, Y. Xu, Q. Weng, X. Jiang, M. Mitome, D. Golberg, Y. Bando, Nat. Commun. 4 (2013) 2905–2912.
[18] S.L. Chen, G.H. He, H. Hu, S.Q. Jin, Y. Zhou, Y.Y. He, S.J. He, F. Zhao, H.Q. Hou, Energy Environ. Sci. 6 (2013) 2435–2439.
[19] G. Zhu, C. Xi, Y. Liu, J. Zhu, X. Shen, J. Mater. Chem. A 3 (2015) 7591–7599.
[20] T.N. Pham, A. Samikannu, J. Kukkola, A.R. Rautio, O. Pitkanen, A. Dombovari, G. S. Lorite, T. Sipola, G. Toth, M. Mohl, J.P. Mikkola, K. Kordas, Sci. Rep. 4 (2014) 6933–6940.
[21] Z.S. Wu, K. Parvez, X. Feng, K. Müllen, Nat. Commun. 4 (2013) 2487–2494.
[22] J.R. Miller, R.A. Outlaw, B.C. Holloway, Science 329 (2010) 1637–1639.
[23] Y. Gogotsi, P. Simon, Science 334 (2011) 917–918.
[24] P. Simon, Y. Gogotsi, B. Dunn, Science 343 (2014) 1210–1211.
[25] M. Sevilla, A.B. Fuertes, ACS Nano 8 (2014) 5069–5078.
[26] H. Wang, Z. Xu, A. Kohandehghan, Z. Li, K. Cui, X. Tan, T.J. Stephenson, C. K. King'ondu, C.M. Holt, B.C. Olsen, J.K. Tak, D. Harfield, A.O. Anyia, D. Mitlin, ACS Nano 7 (2013) 5131–5141.
[27] J. Wang, L. Shen, P. Nie, X. Yun, Y. Xu, H. Dou, X. Zhang, J. Mater. Chem. A 3 (2015) 2853–2860.
[28] S. He, H. Hou, W. Chen, J. Power Sources 280 (2015) 678–686.
[29] J. Chen, J. Xu, S. Zhou, N. Zhao, C.-P. Wong, Nano Energy 15 (2015) 719–728.
[30] S. Dutta, A. Bhaumik, K.C.W. Wu, Energy Environ. Sci. 7 (2014) 3574–3592.
[31] N.P. Wickramaratne, J. Xu, M. Wang, L. Zhu, L. Dai, M. Jaroniec, Chem. Mater. 26 (2014) 2820–2828.
[32] H. Wang, T. Maiyalagan, X. Wang, ACS Cat. 2 (2012) 781–794.
[33] J. Zhou, J. Lian, L. Hou, J. Zhang, H. Gou, M. Xia, Y. Zhao, T.A. Strobel, L. Tao, F. Gao, Nat. Commun. 6 (2015) 8503–8510.
[34] S. Zhou, J.L. Xu, Y.B. Xiao, N. Zhao, C.P. Wong, Nano Energy 13 (2015) 458–466.
[35] Z.-K. Wu, Z. Lin, L. Li, B. Song, K.-S. Moon, S.-L. Bai, C.-P. Wong, Nano Energy 10 (2014) 222–228.
[36] P. Hao, Z. Zhao, Y. Leng, J. Tian, Y. Sang, R.I. Boughton, C.P. Wong, H. Liu, B. Yang, Nano Energy 15 (2015) 9–23.
[37] E. Haque, M.M. Islam, E. Pourazadi, M. Hassan, S.N. Faisal, A.K. Roy, K. Konstantinov, A.T. Harris, A.I. Minett, V.G. Gomes, RSC Adv. 5 (2015) 30679–30686.
[38] F. Xu, Z. Tang, S. Huang, L. Chen, Y. Liang, W. Mai, H. Zhong, R. Fu, D. Wu, Nat. Commun. 6 (2015) 7221–7232.
[39] Z.-Y. Yang, L.-J. Jin, G.-Q. Lu, Q.-Q. Xiao, Y.-X. Zhang, L. Jing, X.-X. Zhang, Y.-M. Yan, K.-N. Sun, Adv. Funct. Mater. 24 (2014) 3917–3925.
[40] J. Chen, J. Xu, S. Zhou, N. Zhao, C.-P. Wong, J. Mater. Chem. A 3 (2015) 17385–17391.
[41] P. Yang, Y. Ding, Z. Lin, Z. Chen, Y. Li, P. Qiang, M. Ebrahimi, W. Mai, C.P. Wong, Z.L. Wang, Nano Lett. 14 (2014) 731–736.

[42] Z. Su, C. Yang, B. Xie, Z. Lin, Z. Zhang, J. Liu, B. Li, F. Kang, C.P. Wong, Energy Environ. Sci. 7 (2014) 2652–2659.
[43] L. Shen, L. Yu, H.B. Wu, X.Y. Yu, X. Zhang, X.W. Lou, Nat. Commun. 6 (2015) 6694–6701.
[44] H. Xia, C. Hong, B. Li, B. Zhao, Z. Lin, M. Zheng, S.V. Savilov, S.M. Aldoshin, Adv. Funct. Mater. 25 (2015) 627–635.
[45] X. Wu, L. Jiang, C. Long, T. Wei, Z. Fan, Adv. Funct. Mater. 25 (2015) 1648–1655.
[46] H. Li, Y. Gao, C. Wang, G. Yang, Adv. Energy Mater. 5 (2015) 1401767–1401775.
[47] L. Shen, J. Wang, G. Xu, H. Li, H. Dou, X. Zhang, Adv. Energy Mater. 5 (2015) 1400977–1400983.
[48] Z. Zhang, F. Xiao, L. Qian, J. Xiao, S. Wang, Y. Liu, Adv. Energy Mater. 4 (2014) 1400064–1400072.
[49] X. Lu, Y. Zeng, M. Yu, T. Zhai, C. Liang, S. Xie, M.S. Balogun, Y. Tong, Adv. Mater. 26 (2014) 3148–3155.
[50] P. Yang, X. Xiao, Y. Li, Y. Ding, P. Qiang, X. Tan, W. Mai, Z. Lin, W. Wu, T. Li, H. Jin, P. Liu, J. Zhou, C.P. Wong, Z.L. Wang, ACS Nano 7 (2013) 2617–2626.
[51] C. Zhou, Y. Zhang, Y. Li, J. Liu, Nano Lett. 13 (2013) 2078–2085.
[52] G. Sun, X. Zhang, R. Lin, J. Yang, H. Zhang, P. Chen, Angew. Chem. Int. Ed. 54 (2015) 4651–4656.
[53] J. Liu, L. Zhang, H.B. Wu, J. Lin, Z. Shen, X.W. Lou, Energy Environ. Sci. 7 (2014) 3709–3719.
[54] T. Zhai, X.H. Lu, Y.C. Ling, M.H. Yu, G.M. Wang, T.Y. Liu, C.L. Liang, Y.X. Tong, Y. Li, Adv. Mater. 26 (2014) 5869–5875.
[55] W. Chen, C. Xia, H.N. Alshareef, ACS Nano 8 (2014) 9531–9541.
[56] S.J. Peng, L.L. Li, C.C. Li, H.T. Tan, R. Cai, H. Yu, S. Mhaisalkar, M. Srinivasan, S. Ramakrishna, Q.Y. Yan, Chem. Commun. 49 (2013) 10178–10180.
[57] Y.F. Zhang, M.Z. Ma, J. Yang, C.C. Sun, H.Q. Su, W. Huang, X.C. Dong, Nanoscale 6 (2014) 9824–9830.
[58] H.C. Chen, J.J. Jiang, L. Zhang, H.Z. Wan, T. Qi, D.D. Xia, Nanoscale 5 (2013) 8879–8883.
[59] J. Xiao, L. Wan, S. Yang, F. Xiao, S. Wang, Nano Lett. 14 (2014) 831–838.
[60] J. Pu, F.L. Cui, S.B. Chu, T.L. Wang, E.H. Sheng, Z.H. Wang, ACS Sust. Chem. Eng. 2 (2014) 809–815.
[61] S. He, W. Chen, J. Power Sources 262 (2014) 391–400.
[62] V. Augustyn, J. Come, M.A. Lowe, J.W. Kim, P.L. Taberna, S.H. Tolbert, H. D. Abruna, P. Simon, B. Dunn, Nat. Mater. 12 (2013) 518–522.
[63] T. Brezesinski, J. Wang, S.H. Tolbert, B. Dunn, Nat. Mater. 9 (2010) 146–151.
[64] J.Z. Chen, L. Yang, S.H. Fang, S. Hirano, K. Tachibana, J. Power Sources 200 (2012) 59–66.
[65] L. Yu, L. Zhang, H.B. Wu, X.W. Lou, Angew. Chem. Int. Ed. 53 (2014) 3711–3714.
[66] J. Pu, T. Wang, H. Wang, Y. Tong, C. Lu, W. Kong, Z. Wang, ChemPlusChem 79 (2014) 577–583.
[67] H. Wang, Y. Liang, M. Gong, Y. Li, W. Chang, T. Mefford, J. Zhou, J. Wang, T. Regier, F. Wei, H. Dai, Nat. Commun. 3 (2012) 917–924.
[68] J. Liu, M. Chen, L. Zhang, J. Jiang, J. Yan, Y. Huang, J. Lin, H.J. Fan, Z.X. Shen, Nano Lett. 14 (2014) 7180–7187.

Jizhang Chen received his B. S. degree of Chemical Enginerring and pH. D degree of Applied Chemistry from Shanghai Jiaotong University in 2009 and 2014, respectively. He is currently a postdoc in the group of Prof. Ching Ping Wong and Prof. Ni Zhao at the Chinese University of Hong Kong. His research interest includes aqueous energy storage devices.

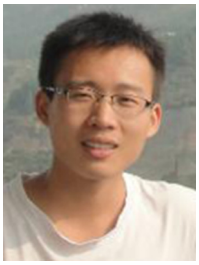

Junling Xu received his B. E. degree from University of Jinan in 2010 and M. E. degree from Shandong University in 2012. Now he is a pH. D candidate in Department of Electronic Engineering at the Chinese University of Hong Kong under the supervision of Professor Ching Ping Wong and Professor Ni Zhao. He is currently studying the diffusion/migration process and kinetics of electrode reaction for electrochemical energy storage cells.

Shuang Zhou received her B. S. degree in Department of Chemistry from Tsinghua University, China. Since 2011, she continued her study on graphene-based electronics and energy storage applications under the supervision of Prof. Ching-Ping Wong and Prof. Ni Zhao, and is now a pH. D candidate in Department of Electronic Engineering, the Chinese University of Hong Kong.

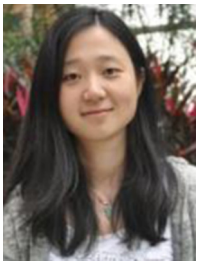

Ni Zhao received her B. Eng. degree from Tsinghua University and M. S. degree from McMaster University. In 2008, she received her pH. D degree in Physics from the University of Cambridge. From 2008 to 2010 she worked as a postdoctoral research fellow at the Massachusetts Institute of Technology. She joined the Department of Electronic Engineering at the Chinese University of Hong Kong in Dec. 2010. Her current research interests include optoelectronic, electronic and electrochemical devices based on organic and nanostructured materials.

Ching-Ping Wong is Dean of Engineering Faculty at the Chinese University of Hong Kong and a Regents' Professor at Georgia Institute of Technology. Prior to that, he was with AT&T Bell Laboratories for many years and was an AT&T Bell Laboratories Fellow. His research interests focus on the areas of material and process for electronic, photonic, MEMS, sensors, energy harvesting and storage. He has published over 1,000 technical papers and 12 books, and holds over 65 US Patents. He is a member of the US National Academy of Engineering and a Foreign Academician of the Chinese Academy of Engineering.